Mechanical Deformation of High-Impact Polystyrene under Uniaxial Tension at Various Strain Rates

Takashi Kuboki,*,† P.-Y. Ben Jar,‡ Kiyoshi Takahashi,† and Tetsuya Shinmura§

Research Institute for Applied Mechanics, Kyushu University, 6-1 Kasuga-koen, Kasuga, Fukuoka 816-8580, Japan; Department of Mechanical Engineering, University of Alberta, Edmonton, Alberta T6G 2G8, Canada; and Research & Development Department, Chiba Plant, Denki Kagaku Kogyo Company, Limited, 6 Goiminamikaigan, Ichihara, Chiba, 290-0045, Japan

Received May 30, 2001

ABSTRACT: Tensile properties of two high-impact polystyrenes (HIPS), named 0.84S and 0.45S, were evaluated at four strain rates, from 2.7×10^{-3} to 1.8×10 s^{-1}, using un-notched dumbbell specimens. Under the strain rates up to 1.6×10^{-1} s^{-1}, 0.84S showed slightly higher fracture energy than 0.45S, where the fracture energy is defined as the total area under the force−displacement curve. However, when the strain rate was further increased to 1.8×10 s^{-1}, the difference was remarkably increased, due to a dramatic increase of the fracture energy for 0.84S at the highest strain rate, 1.8×10 s^{-1}. The high fracture energy for 0.84S was found to come mainly from the fracture strain. The microscopic examination, using optical microscopy and transmission electron microscopy (TEM), shows the trend of deformation behavior, which supports the tensile test results, and suggests that the adiabatic deformation process, which has long been known to cause the fracture energy increase at high strain rates for many polymers, does not provide a satisfactory explanation for the results presented here. Instead, it is believed that at the highest strain rate the molecular stretch, instead of the molecular flow, dominated the craze fibril deformation and resulted in the craze proliferation around the rubber particle. Such a craze proliferation mechanism did not occur in 0.45S, because unlike 0.84S, the displacement misfit between particle and matrix was insufficient to initiate crazes. As a result, the fracture strain and the fracture energy were limited. We conclude from the study that the different capability to initiate crazes is a dominant factor for the significantly different fracture energy of the two HIPS at the highest strain rate.

1. Introduction

High-impact polystyrene (HIPS), due to its versatility for a wide range of applications, has long been studied to understand the dependence of its mechanical properties on the constituent polymers and the loading conditions. The former includes molecular weight of the matrix and properties of the rubber particles (such as rubber content, rubber particle size, rubber particle structure, and rubber cross-link density), and the latter includes service temperature, strain rate, and fracture behavior under various stress states.[1,2] Among those parameters, the strain rate was expected to have a significant effect on the mechanical properties, mainly due to the viscoelastic nature of the polymer deformation. However, only limited information on the strain rate effect is available in the literature, because such a study requires various experimental techniques that are not readily available in most laboratories. The mechanical testing requires devices that are capable of introducing high strain rates and equipped with high-speed data acquisition systems for recording the force and elongation, and the deformation analysis requires various sample preparation techniques for optical microscopy and transmission electron microscopy (TEM). For HIPS, the study is also hindered by the large fracture strain of which the range cannot be measured reliably using a strain gauge or a mechanical extensometer. It has long been believed that only a noncontact device can measure the large deformation encountered in the HIPS testing. Unfortunately, most of the commercially available noncontact devices do not have a reliable high-frequency data acquisition capability that is required for the deformation measurement at the high strain rate.

Recently Beguelin et al.[3,4] developed an optical-fiber extensometer that is suitable for the measurement of large deformation under either static or dynamic loading. The extensometer has a gentle contact with the specimen to eliminate the possibility of premature fracture at the contact point and provides a high-frequency response at rates more than 100 kHz.[5]

Using the optical-fiber extensometer and with our experience on the microscopy, mechanical properties and deformation behavior of HIPS at various strain rates were evaluated. The strain rates covered in the study are from 2.7×10^{-3} s^{-1} (pseudo-static) to 1.8×10 s^{-1} (low-speed impact). The associated deformation behavior was examined through the post-fractured specimens using optical microscopy and TEM.

2. Experimental Section

2.1. Materials. Two HIPS (named 0.84S and 0.45S) were used in the study, both having 8 wt % butadiene. The former contains rubber particles with an average diameter of 0.84 μm and the latter 0.45 μm, thus named 0.84S and 0.45S, respectively. As shown in Figure 1, the two HIPS have rubber particles that contain core−shell inclusions of similar size (around 0.15 μm in diameter), and polystyrene matrix of the similar weight-average molecular weight (225 300 and 239 500 for 0.84S and 0.45S, respectively). Therefore, the main difference between the two HIPS is the rubber particle size. Information of the constituent polymers for the two HIPS is summarized in Table 1.

2.2 Mechanical Tests. Injection-molded dumbbell specimens, with dimensions shown in Figure 2, were tested using

† Kyushu University.
‡ Department of Mechanical Engineering, University of Alberta, Edmonton, Alberta T6G 2G8, Canada
§ Denki Kagaku Kogyo Co., Ltd.

10.1021/ma0109424 CCC: $22.00
Published on Web 03/16/2002

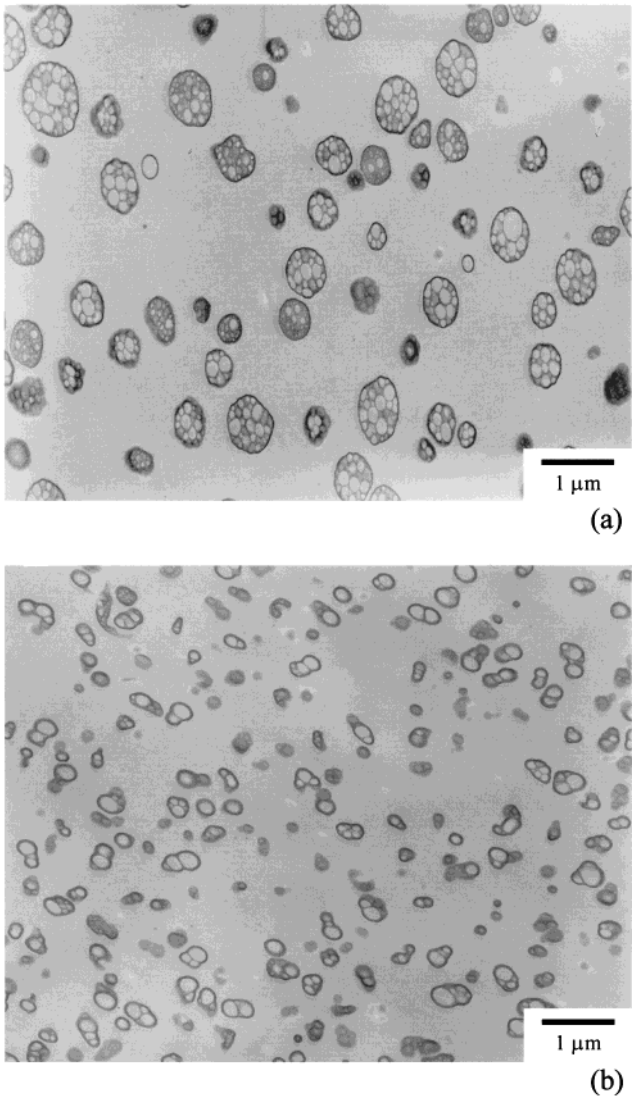

Figure 1. Morphology of the HIPSs: (a) 0.84S and (b) 0.45S.

Table 1. Material Information of the HIPS Used in This Study

material	composition (wt %) St[a]	composition (wt %) Bd[b]	wt-av mol wt of PS[c]	av size of particles (μm)	morphology of individual inclusion
0.84S	92	8	225 300	0.84	core−shell
0.45S	92	8	239 500	0.45	core−shell

[a] St: styrene. [b] Bd: butadiene. [c] PS: polystyrene.

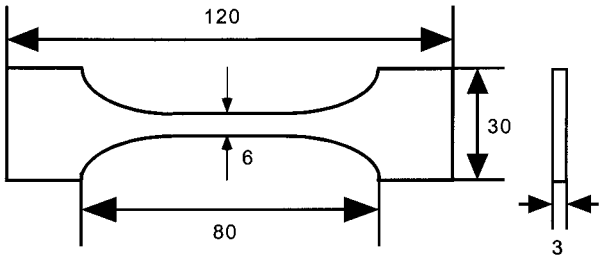

Figure 2. Specimen geometry and dimensions (in mm) used for the tensile testing.

a Shimazu servohydraulic testing machine (model EHF-FD1-10LA) for strain rates up to 1.6×10^{-1} s^{-1} and an in-house-built falling-weight impact tensile testing machine[6] at the highest strain rate, 1.8×10 s^{-1}.

Figure 3a depicts the schematic diagram of the falling-weight impact tensile test machine. The machine uses a striker

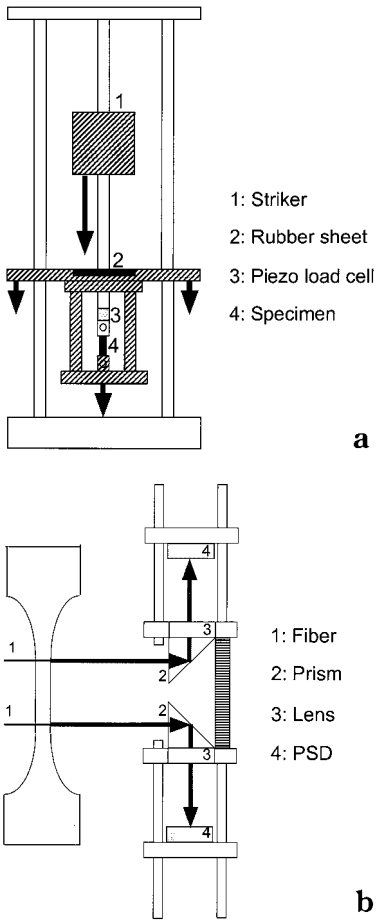

Figure 3. In-house-built devices for the mechanical testing: (a) Schematic diagram of the falling-weight impact tensile test machine; (b) depiction of the optical-fiber extensometer setup for the elongation measurement.

of 10 kg to impact on the lower crosshead assembly (the parts shaded in Figure 3a) to introduce the deformation. A rubber sheet of 8 mm thick was placed on the contact area between the striker and the lower crosshead assembly to reduce oscillation of the force signals that was induced by the impact loading. The impact force was measured using a piezoelectric load cell attached to the upper crosshead.

Setup of the optical-fiber extensometer for the elongation measurement in tensile tests is depicted in Figure 3b, similar to that developed by Beguelin.[3,4] Two fibers of 250 μm in diameter were gently placed in parallel in the gauge section of the specimens using a double-sided adhesive tape. Laser light emitted from each of the optical fiber passes through a prism, and is focused on a position sensitive detector (PSD). The initial distance between the two optical fibers, which corresponds to the initial gauge length for the elongation measurement, was 25 mm.

An example of the data collected from a 0.84S specimen using the falling-weight impact tensile test machine is shown in Figure 4 that contains the time function of the displacement signals from the two optical fibers and the force signals from the piezoelectric load cell. Oscillation was observed in all of the curves, especially in the force curve. The oscillation indicates the dynamic loading effect, due to vibration and stress wave propagation. Specimen elongation, also shown in the figure, was obtained by subtracting the upper fiber displacement from the lower fiber displacement. It was found that the slope of the curve for the upper fiber displacement, representing the vertical speed of the upper fiber, was greatly decreased at the onset of yielding. In contrast, the slope of the curve for the lower fiber displacement only showed a small change. This is because after the yield point, elongation mainly occurred within the gauge section between the two optical

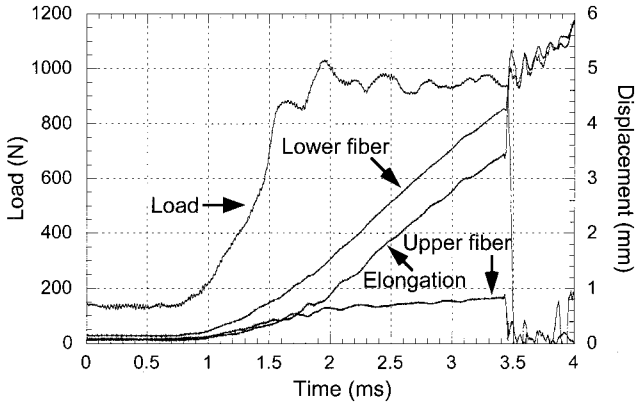

Figure 4. Example of the results obtained from the falling-weight impact tensile test machine. The material used was 0.84S, and the corresponding strain rate was $1.8 \times 10\ s^{-1}$.

fibers. When fracture occurred, around $t = 3.4$ ms in Figure 4, all signals showed a sudden change in value.

Reliability of the optical-fiber extensometer under a high strain rate has been previously examined by comparing the measured values with those from a strain-gauge-based extensometer and those from a high-speed camera.[7] The results show that the optical-fiber extensometer has satisfactory precision for the measurement, even for large deformations.

2.3. Microscopic Examination of the Deformation Behavior. Optical microscopy and TEM were used to examine the deformation behavior. The optical micrographs were taken from the fractured specimens under the transmitted light using a general-purpose camera equipped with a microzoom lens (Micro-Nikkor by Nikon). The TEM samples were prepared from regions near the fracture surface in order to examine the deformation behavior immediately underneath the fracture surface. The TEM samples were prepared by staining the fractured specimens in the vapor of an OsO_4 solution of 2 wt % for 48 h, which were then sliced to thin sections of approximately 100 nm thick using an ultramicrotome (Reichert Jung Ultracut) equipped with a Diatome diamond knife. Details of the TEM sample preparation can be found in ref 8. A Hitachi H7100 TEM operated at 75 kV was used for the deformation observation.

3. Results

3.1. Mechanical Tests. The typical stress−strain curves for the two HIPS under various strain rates are shown in Figure 5. At the highest strain rate of $1.8 \times 10\ s^{-1}$, as expected, oscillation was observed from both 0.84S (Figure 5a) and 0.45S (Figure 5b), especially in the section beyond the elastic limit. The oscillation was eliminated by modifying the curves based on the oscillation center, defined as the mean of the adjacent oscillating stress values. Using the modified curves, the maximum stress values at the highest strain rate were determined. The curves also provide values for Young's modulus during the initial elastic deformation, strain at the onset of fracture (named fracture strain hereafter), and fracture energy that is the total area under the force−displacement curve. These values are plotted vs the strain rate in Figure 6.

In Figure 6a, both HIPS showed that the Young's modulus decreases slightly with the increase of the strain rate, except for 0.45S in the low strain rate range. However, the overall variation is very small in view of the uncertainty due to the data scattering. The curve of the maximum stress vs the strain rate is shown in Figure 6b, in which both HIPS show that the maximum stress increases linearly with the increase of the logarithmic strain rate. At any given strain rate, 0.45S shows a higher maximum stress than does 0.84S.

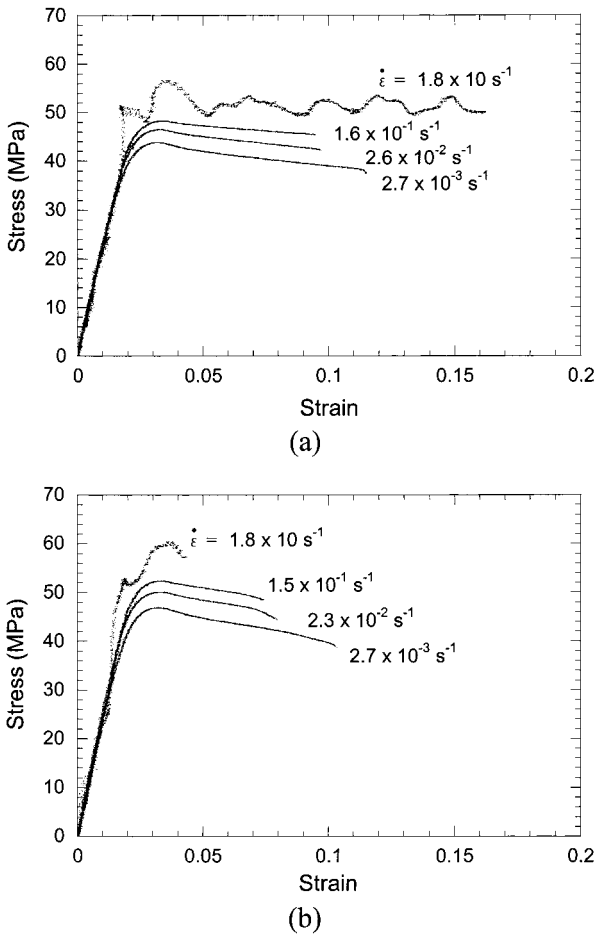

Figure 5. Typical stress−strain curves under various strain rates for (a) 0.84S and (b) 0.45S. Numbers next to the curve are the strain rates used in the tests.

Despite the similarity in the strain rate dependence between the Young's modulus and the maximum stress, the two HIPS show different strain rate functions for the fracture strain and the fracture energy, as shown in Figure 6c and 6d. The two properties for 0.45S continuously decrease with the increase of the strain rate, whereas those for 0.84S show a U-shaped trend with an initial decrease at the low strain rate range (from 2.7×10^{-3} to $2.5 \times 10^{-2}\ s^{-1}$) and an increase at the high strain rate range. The increase was more than 60% when the strain rate increased from 1.6×10^{-1} to $1.8 \times 10\ s^{-1}$. It should be noted that the values at the highest strain rate of $1.8 \times 10\ s^{-1}$ are even higher than those measured at the lowest strain rate of $2.7 \times 10^{-3}\ s^{-1}$. It should also be noted that in contrast to the maximum stress, the fracture strain and the fracture energy for 0.84S are always higher than those for 0.45S. The curves in Figure 6, parts c and d, suggest that the variation of the fracture energy follows very closely to the variation of the fracture strain. This leads us to conclude that the significant increase of the fracture energy for 0.84S under the impact loading is mainly due to the increase of the fracture strain.

The strong correlation between the fracture strain and the fracture energy was further investigated by examining the residual plastic strain in the fractured specimens, based on the length variation of gauge section. The residual plastic strains for 0.84S show a gradual decrease with the increase of the strain rate, being the values of 0.045, 0.042, 0.035, and 0.031 for strain rates of 2.7×10^{-3}, 2.5×10^{-2}, 1.6×10^{-1}, and

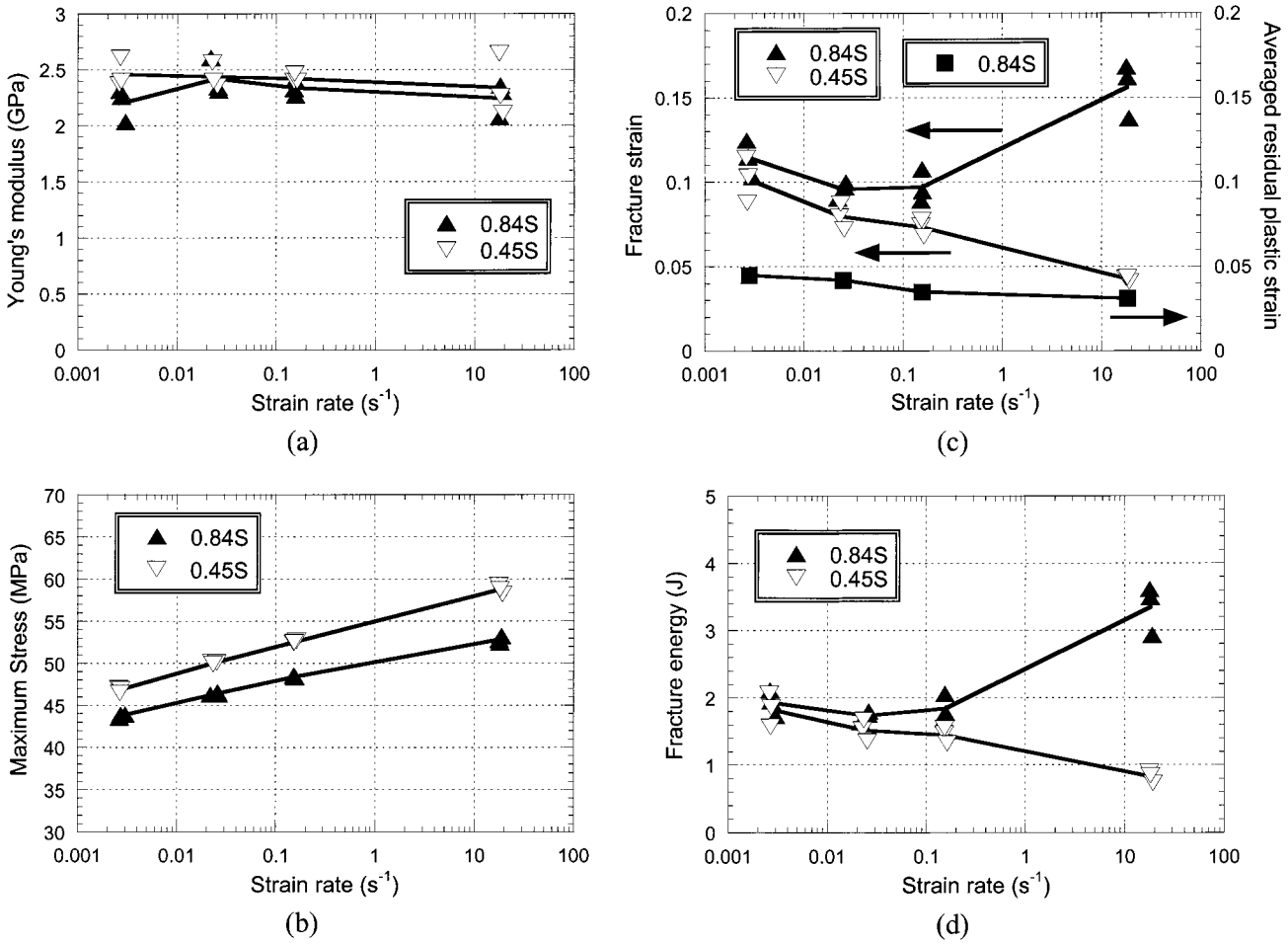

Figure 6. Summary of the mechanical test results vs the strain rate: (a) Young's modulus; (b) maximum stress; (c) fracture strain and residual plastic strain; (d) fracture energy.

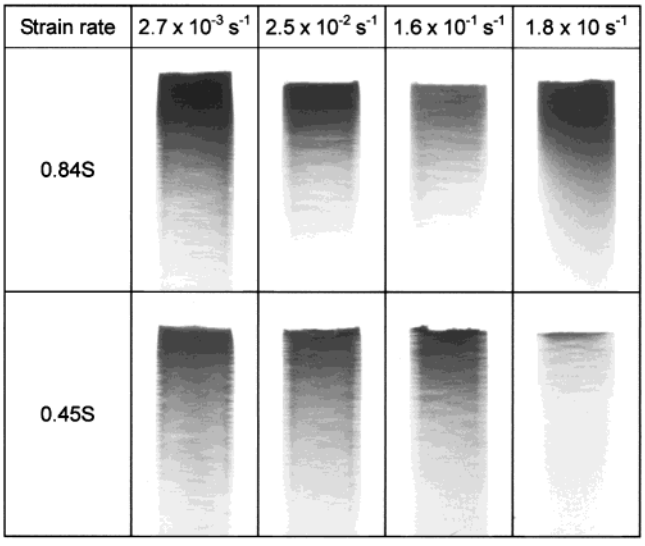

Figure 7. Transmission optical micrographs of specimens fractured at various strain rates.

$1.8 \times 10\ s^{-1}$, respectively, as shown in Figure 6c. The trend of variation is different from that of the fracture strain.

3.2. Optical Microscopy. Optical micrographs of the stress-whitening zone for the HIPS at all strain rates are presented in Figure 7. The stress-whitening zone is a phenomenon generated from the plastic deformation, and appears to be darker than the un-deformed region in Figure 7 due to opacity of the zone. Size of the stress-whitening zone for 0.45S appears to continuously decrease with the increase of the strain rate, which is consistent with the variation of the fracture strain. Such consistency is also found between the whitening zone size and the fracture strain for 0.84S. As shown in Figure 7, size of the stress-whitening zone for 0.84S first decreases with the increase of the strain rate from 2.7×10^{-3} to $1.6 \times 10^{-1}\ s^{-1}$, and then significantly increases when the strain rate is further increased to $1.8 \times 10\ s^{-1}$. However, due to the difficulties in defining the size of the stress-whitening zone, the information provided by the optical micrographs can only be used as qualitative evidence to support the mechanical test results, namely, the unusual increase of the fracture strain and the fracture energy for 0.84S at the highest strain rate.

In contrast to its consistency with the fracture strain and the fracture energy, the stress-whitening zone size does not show any correlation with the residual plastic strain.

3.3. TEM. Plastic deformation in HIPS is known to come mainly from crazing.[9−15] Therefore, a strong relationship is expected to exist between the macroscopic deformation of HIPS and its microscopic crazing behavior. The TEM study enabled us to compare number and width of the crazes in regions near the fracture surface, in search for additional information on the deformation mechanisms to support the mechanical test results in Figure 6, parts c and d.

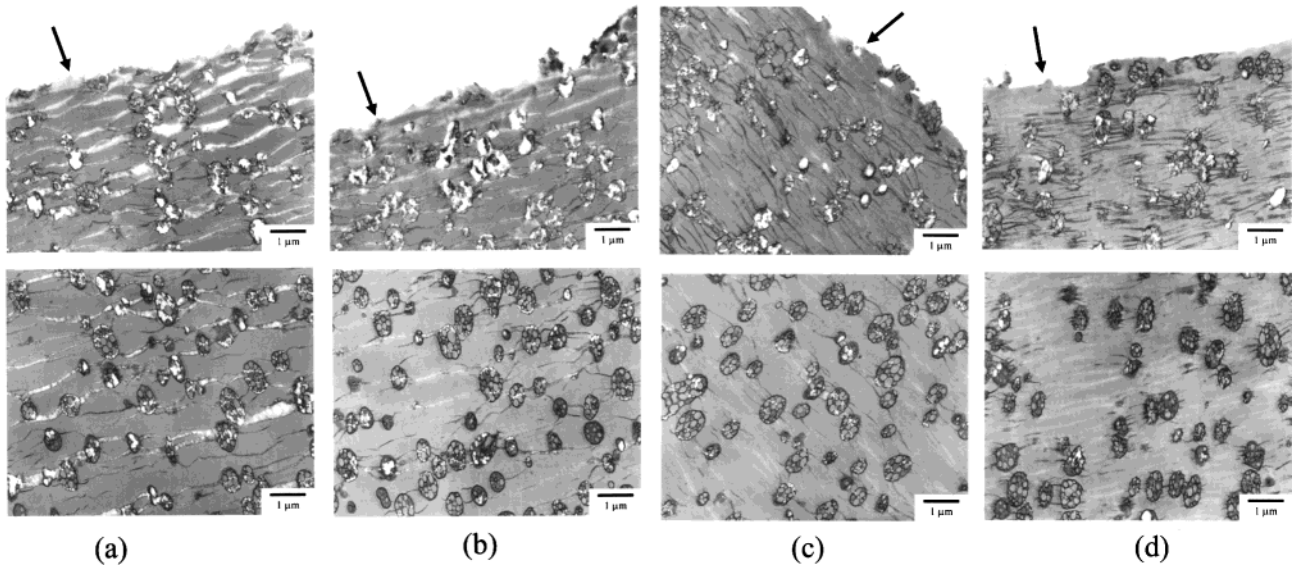

Figure 8. TEM micrographs of 0.84S under various strain rates: (a) 2.7×10^{-3} s^{-1}; (b) 2.5×10^{-2} s^{-1}; (c) 1.6×10^{-1} s^{-1}; (d) 1.8×10 s^{-1}. Top micrographs were taken from regions near the fracture surface, in which the arrow indicates where the fracture surface is and is oriented to be parallel to the loading direction, and the bottom micrographs from regions of 30 μm away from the fracture surface.

Figure 8 summarizes the TEM micrographs of 0.84S fractured at all strain rates. The top micrographs were taken from regions immediately underneath the fracture surface. An arrow is used in the top micrographs to point to the fracture surface. In addition, the arrow is oriented to align with the tensile loading direction. The bottom micrographs were taken from regions of 30 μm away from the fracture surface. Micrographs in Figure 8a, taken from specimens fractured at the strain rate of 2.7×10^{-3} s^{-1}, show many highly deformed, widely open crazes in which some of the craze fibrils have already broken down. These micrographs indicate that the crazes had been well developed in the specimens before the fracture occurred and that the fracture was initiated by the coalescence of the crazes. The micrographs from specimens fractured at the intermediate low strain rate, 2.5×10^{-2} s^{-1}, are shown in Figure 8b. These micrographs seem to show a similar number of crazes to that in Figure 8a, but each craze has slightly smaller opening width. The micrographs in Figure 8c were taken from specimens fractured at the intermediate high strain rate, 1.6×10^{-1} s^{-1}. Compared with those in Figure 8b, the micrographs in Figure 8c show a slight increase in craze number but a decrease in craze opening width. The crazes in Figure 8c include white crazes of which the low contrast with the matrix came from the insufficient OsO_4 staining.[16] Figure 8d shows TEM micrographs for specimens fractured at the highest strain rate, 1.8×10 s^{-1}. Crazes in Figure 8d have similar opening width with those in Figure 8c, but the number of crazes initiated from each rubber particle in Figure 8d has been much increased. The percentage of white crazes in Figure 8d is also greatly increased in the region of 30 μm away from the fracture surface. Despite the large percentage of crazes being white crazes, most crazes in the region immediately beneath the fracture surface in Figure 8d appear to be black crazes of which the length is shorter than that has been expected, especially in view of the interparticle distance and the large strain at the onset of fracture.

Figure 9 shows TEM micrographs of 0.45S specimens fractured at the lowest strain rate of 2.7×10^{-3} s^{-1} and the highest strain rate of 1.8×10 s^{-1}. Again, micrographs were taken from regions immediately beneath the fracture surface and 30 μm away from the fracture surface. Many highly deformed crazes are shown in Figure 9a, some of which have already broken down, especially in regions just beneath the fracture surface. Craze opening width in Figure 9a is similar to that in Figure 8a, but the total number of crazes in Figure 9a is bigger. This is probably due to the smaller particle size of 0.45S. When the number of crazes is normalized by the number of rubber particles, i.e., the number of crazes per rubber particle, the two micrographs, Figure 8a and 9a, show similar behavior. Figure 9b was taken from specimens fractured at the highest strain rate of 1.8×10 s^{-1}. The micrographs show that crazes are generated only from some of the rubber particles,

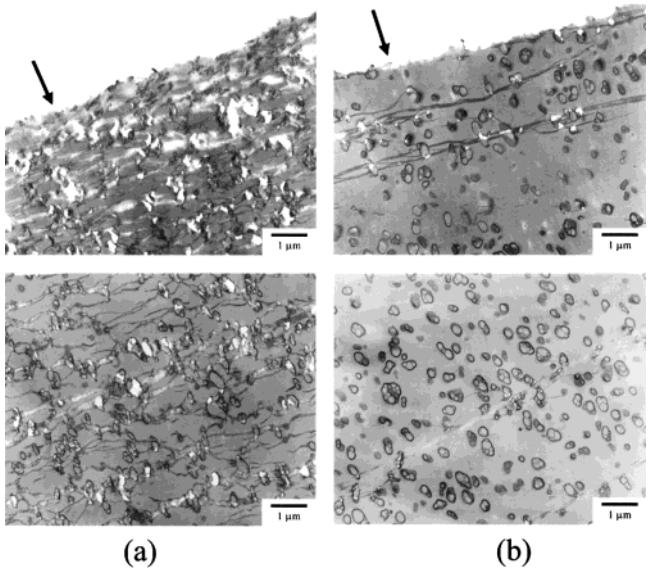

Figure 9. TEM micrographs of 0.45S under various strain rates: (a) the lowest strain rate of 2.7×10^{-3} s^{-1} and (b) the highest strain rate of 1.8×10 s^{-1}. The top micrographs were taken from regions near the fracture surface, in which the arrow indicates where the fracture surface is and is oriented to be parallel to the loading direction, and the bottom micrographs from regions of 30 μm away from the fracture surface.

supporting the relatively brittle fracture shown in Figure 5b. White crazes were also found in the region of 30 μm away from the fracture surface, but the number is much smaller than that in Figure 8d (for 0.84S) under the same strain rate.

4. Discussion

The mechanical behavior is largely expected based on our current understanding of the strain rate effect, except for the significant increase of the fracture strain and the fracture energy for 0.84S at the highest strain rate, $1.8 \times 10\ s^{-1}$. We have eliminated the possibility of the increase in the fracture strain coming from the use of the new falling-weight impact tensile testing machine, as the unexpected increase at the highest strain rate was only observed in 0.84S and not in 0.45S. Besides, optical micrographs in Figure 7 support the significant increase of the deformation in 0.84S at the highest strain rate. What is not clear is why only 0.84S and not 0.45S showed the significant increase.

4.1. Possibility of Adiabatic Deformation. Most polymers are known to show the trend of ductility decreasing with the increase of the strain rate until a critical strain rate is reached, beyond which the trend may be reversed. For example, Dijkstra et al.[17] observed the increase of ductility for nylon-6/ethylene−propylene rubber (EPR) blends at sufficiently high strain rates and suggested that a transition from isothermal deformation to adiabatic deformation has occurred, in which the heat generated blunted the crack tip, thus slowing down the crack propagation and increasing the fracture energy. Microscopic observation of three-layered structure under the fracture surface, which shows noticeably different deformation behavior, has provided supporting evidence to the adiabatic deformation process.[17,18] The first layer, within 3−5 μm from the fracture surface, showed no cavitation or any evidence of deformation and was only observed in specimens tested at the high strain rate. This layer was suggested to be the result of a melt-resolidification process that had been caused by the heat generated in the local adiabatic deformation.

Fracture energy increase with the increase of the strain rate was also observed in blends of polypropylene and ethylene−propylene−diene monomer (PP/EPDM)[19] and poly(acrylonitrile−butadiene−styrene) (ABS).[20] A similar melt-resolidified layer was observed immediately beneath the fracture surface, in which no evidence of deformation was present. The adiabatic deformation process results in the crack tip blunting that increases the fracture energy for these materials.[19,21]

Increase of fracture energy for HIPS under a high strain rate, similar to the increase reported here, was first observed by Vu-Khanh.[22] Its main difference from the current study is that Vu-Khanh used the three-point bend tests on notched HIPS specimens, instead of the tensile test on the un-notched specimens. They suggested that the adiabatic-deformation-induced crack tip blunting be the cause of the fracture energy increase in the HIPS. However, unlike the other work, no deformation mechanisms were examined to support the suggestion.

In the current study, the TEM micrographs for the two HIPS did not show any evidence to support the occurrence of the melt-resolidification during the fracture process. Therefore, the adiabatic deformation process cannot satisfactorily explain the large increase in the fracture strain and the fracture energy for 0.84S at the high strain rate. It should be noted that the strain rate used in our study is lower than that used by Vu-Khanh. Therefore, the adiabatic deformation could have occurred in our specimens if the strain rate was high enough. However, further study is required to support this speculation.

4.2. Deformation Recovery. As shown in Figure 6c, the fracture strain of the HIPS specimens is significantly larger than the residual plastic strain. For 0.84S tested at the highest strain rate ($1.8 \times 10\ s^{-1}$), the fracture strain is 0.156 and the residual plastic strain is 0.031. That is, excluding the elastic strain of about 0.03 (estimated from Figure 5a), over 75% of the fracture strain has been recovered after the fracture. Such deformation recovery is known to occur in polymers under the impact loading.[23,24] As the crazing is the dominant deformation mechanism, the deformation recovery process should be closely related to the craze healing that was firstly reported by Takahashi,[23] who suggested that the instant disappearance of stress whitening in fractured ABS/methyl methacrylate (MMA) blend under the impact loading is due to the rapid healing of the crazes, leading to the recovery of the plastic deformation. The deformation recovery also occurred in 0.45S at the same strain rate. However, the amount of the strain recovery could not be measured accurately due to the small fracture strain values.

Deformation recovery of polymers can also occur under static loading, and has been reported before.[25] Results from the current study show that the recovery of plastic strain has occurred even under the lowest strain rate of $2.7 \times 10^{-3}\ s^{-1}$. For example, 0.84S specimens tested at this strain rate showed a value of 0.114 for the fracture strain and 0.045 for the residual plastic strain. Excluding the elastic strain of around 0.03, as suggested in Figure 5a, a plastic strain of about 0.04 (50% of the total plastic strain) has been recovered after the fracture.

4.3. Deformation of Craze Fibrils. The above analysis indicates that the deformation recovery has occurred in both HIPS at all strain rates, and the amount of the deformation recovery increases with the increase of the strain rate. Crazing is known to involve stretch[26] and flow[27−31] of polymeric molecules. Stretch is the deformation of molecular sections between entanglements, and flow is a disentanglement process. Increase of the strain rate reduces the time for the crazes to respond to the deformation, thus the molecules involved are in favor of the stretch rather than the flow. As long as chain scission does not occur, the molecular stretch tightens the entanglements and increases the strength of the crazes to resist further deformation. This in turn increases the recovery force when the fracture occurs. A sufficient recovery can lead to craze healing and ultimately decrease the whitening zone size. The reduction of craze flow in the deformation process by increasing the strain rate also strengthens the craze fibrils, thus preventing early fibril breakdown. This is expected to facilitate the craze proliferation around each particle.

4.4. Key Parameter for the Different Fracture Strains at the Highest Strain Rate. Although the strengthening of craze fibrils seems to be a reasonable explanation for 0.84S showing significant craze proliferation at the highest strain rate, it cannot be applied to 0.45S which, as shown in Figure 9b, shows that the craze population is dramatically reduced at this strain

rate. Such a different trend in the craze generation must have come from the two main differences between the two HIPS, that is, the weight-average molecular weight of polystyrene (225 300 and 239 500 for 0.84S and 0.45S, respectively) and the average particle size (0.84 μm and 0.45 μm in diameter). However, the small difference in the molecular weight is expected to have a negligible effect on the mechanical properties. Furthermore, the fact that the 0.84S with polystyrene of lower molecular weight shows higher fracture strain provides no support to the molecular weight effect on its high fracture strain. Therefore, we believe that the main difference in the material parameters that has caused the increase of the fracture strain for 0.84S is related to the difference of the particle size, though the two HIPS actually have very small difference in the particle size, compared to the particle size difference used in the previous studies.[32,33]

For HIPS, critical particle size (D_c) is well-known to exist, below which the mechanical toughness becomes very poor.[34−38] Argon et al.[39] have suggested that particles smaller than D_c cannot generate sufficient displacement misfit between the particle and the matrix to initiate crazes, thus showing poor toughness. Piorkowska et al.,[33] using the displacement misfit criterion, have determined that the D_c values for most HIPS systems should be in the range 0.4−0.8 μm. The two HIPS used in the current study are naturally expected to have D_c values in this range, but on the basis of the work by Piorkowska et al.,[33] the D_c for 0.45S may be slightly smaller than that for 0.84S because the former has the higher maximum stress than the latter, as shown in Figure 6b. The smaller D_c value for 0.45S has, to some extent, compensated its smaller average particle size for the craze initiation. As a result, fracture strain for 0.45S is only slightly lower than that for 0.84S, at least for the strain rates up to 1.6×10^{-1} s^{-1}.

At the highest strain rate, 1.8×10 s^{-1}, particles in 0.45S are no longer effective to initiate crazes. This is probably because at the highest strain rate the displacement misfit between particle and matrix in 0.45S is no longer sufficient to initiate the crazes. In other words, we believe that the D_c value is strain-rate-dependent. Higher the strain rate is, larger the D_c value should be, due to the increase of the particle stiffness. As a result, the increase of the craze fibril strength by molecular stretch, instead of molecular flow, cannot be effective to increase the craze population in 0.45S. Should the 0.45S have a larger particle size so that the displacement misfit at the highest strain rate is still big enough to initiate crazes, strengthening of the craze fibrils by the molecular stretch would have increased the number of crazes generated from each particle, thus increasing the fracture strain. This, however, requires further study to verify.

4.5. White and Black Crazes. Another interesting phenomenon in the results is the variation of the length distribution between the white crazes and the black crazes. As suggested by Brown et al.,[40] the black crazes may result from the staining of unsaturated rubber molecules that diffused into the crazes during the craze growth. Without the presence of the rubber molecules, the color of the crazes should remain white and should not be affected by the staining process.[16] Therefore, the observation of white crazes in 0.84S and 0.45S in specimens tested at the high strain rates, especially in regions of 30 μm away from the fracture surface, as shown in Figure 8, parts c and d, for 0.84S and Figure 9b for 0.45S, is an indication of the low mobility of the unsaturated polybutadiene molecules in the rubber particles. Piorkowska et al.[41] suggested that the mobility of the polybutadiene molecules depends on the strain rate, and when the strain rate reaches a critical value, the mobility of the polybutadiene molecules could not keep up with the craze growth rate, resulting in a craze that does not contain rubber molecules in its full length. This concept is supported by our study in which the white crazes were only observed from specimens tested at the high strain rates.

Although we did not intentionally introduce free low-molecular-weight polybutadiene molecules in the rubber particles, it is expected that the low-degree of polymerization of the rubber particles has left some free polybutadiene molecules that are not cross-linked. The free polybutadiene molecules were diffused into the crazes during the deformation process, and created the contrast between the crazes and the surround matrix.

However, the above concept cannot explain why almost all crazes in regions immediately beneath the fracture surface, even under the highest strain rate, are black crazes; while at a short distance away from the fracture surface, such as 30 μm, plenty of white crazes are visible, as shown in Figure 8d and Figure 9b. We believe that rubber molecules that generated black crazes in the stained samples immediately beneath the fracture surface were not diffused into the crazes during the craze growth. Instead, the rubber molecules were transferred to the crazes during the deformation recovery after the specimen was fractured. During the deformation recovery, rubber particles nearby the fracture surface are expected to be under compressive stress that may have squeezed the rubber molecules into the crazes. Supporting evidence for this mechanism is currently under investigation.

5. Conclusions

Mechanical properties and the deformation behavior of two HIPS (0.84S and 0.45S) were evaluated as a function of the strain rate using un-notched dumbbell specimens. The mechanical test results show that the fracture energy of 0.84S can significantly increase when the strain rate is 1.8×10 s^{-1}. The increase of the fracture energy was mainly due to the increase of the fracture strain. The results also showed that the difference in fracture energy between 0.84S and 0.45S, especially at the highest strain rate, is mainly due to the difference in particle size.

The TEM examination on the post-fractured specimens suggests that crazing is the dominant deformation mechanism in both 0.84S and 0.45S at all strain rates. However, the opening width and the number of crazes generated from each rubber particle vary with the strain rate.

The TEM micrographs also show that the significant difference in fracture energy between 0.45S and 0.84S at the highest strain rate was mainly caused by the difference in the number of crazes. The study supports the existence of a strong correlation between the micro-deformation mechanism and the macromechanical behavior of the HIPS, and concludes that the adiabatic deformation process is not the only possible explanation for the high fracture energy of HIPS at a high strain rate.

Despite the fact that the two HIPS have a relatively small difference in the average particle size, the differ-

ence may have been the major factor for the different fracture strain and fracture energy at the highest strain rate. The relatively large particles in 0.84S were able to generate sufficient displacement misfit at the highest strain rate. With the stretch mechanism to increase the craze fibril strength, number of crazes in the 0.84S was significantly increased, resulting in the high fracture strain and fracture energy. The small particle size in 0.45S was probably not able to generate sufficient displacement misfit to initiate crazes. As a result, the 0.45S showed low craze density at the highest strain rate, resulting in the low fracture strain and fracture energy.

Acknowledgment. The authors would like to thank T. Mada at Kyushu University for assistance with the tensile tests and S. Stowe in the Electron Microscope Unit, The Australian National University, for assistance with the TEM. Kuboki also acknowledges the financial support from Targeted Institutional Links Program (administered by DETYA, Australia) and the Japan Society for the Promotion of Science for scholarship support.

References and Notes

(1) Bucknall, C. B. *Toughened Plastics*; Applied Science Publishers: London, 1977.
(2) Kinloch, A. J.; Young, R. J. *Fracture Behaviour of Polymers*; Applied Science Publishers: London and New York, 1983.
(3) Beguelin, Ph.; Barbezat, M.; Kausch, H. H. *J. Phys. (Paris)* III **1991**, *1*, 1867.
(4) Beguelin, Ph. In *Impact Fracture of Polymers-Materials Science and Testing Techniques*; Takahashi, K., Yee, A. F., Eds.; Kyushu University Press: Fukuoka, Japan, 1992; p 291.
(5) Mada, T.; Takahashi, K.; Beguelin, Ph.; Aggag, G. *Trans. Jpn. Soc. Mech. Eng.* **1997**, *A63*, 1431 (in Japanese).
(6) Takahashi, K.; Mada, T.; Beguelin, Ph. *Trans. Jpn. Soc. Mech. Eng.* **1998**, *A64*, 2975 (in Japanese).
(7) Kuboki, T.; Mada, T.; Takahashi, K. *Key Eng. Mater.* **2000**, *183*−*187*, 289.
(8) Jar, B. P.-Y.; Wu, Y. R.; Kuboki, T.; Takahashi, K.; Shinmura, T. *J. Mater. Sci. Lett.* **1997**, *16*, 1489.
(9) Bucknall, C. B.; Smith, R. R. *Polymer* **1965**, *6*, 325.
(10) Matsuo, M. *Polymer* **1966**, *7*, 421.
(11) Matsuo, M. *Polym. Eng. Sci.* **1969**, *9*, 206.
(12) Seward, R. J. *J. Appl. Polym. Sci.* **1970**, *14*, 852.
(13) Kambour, R. P.; Russell, R. R. *Polymer* **1971**, *12*, 237.
(14) Keskkula, H.; Schwarz, M.; Paul, D. R. *Polymer* **1986**, *27*, 211.
(15) Michler, G. H. *Polymer* **1986**, *27*, 323.
(16) Kuboki, T.; Jar, P.-Y. B.; Takahashi, K.; Shinmura, T. *Macromolecules* **2000**, *33*, 5740.
(17) Dijkstra, K.; ter Laak, J.; Gaymans, R. J. *Polymer* **1994**, *35*, 315.
(18) Dijkstra, K.; Gaymans, R. J. *J. Mater. Sci.* **1994**, *29*, 3231.
(19) van der Wal, A.; Gaymans, R. J. Presented at 9th International Conference on Deformation, Yield and Fracture of Polymers, Cambridge University, April 1994; poster 60.
(20) Steenbrink, A. C.; Gaymans, R. J.; van der Giessen, E. Presented at 9th International Conference on Deformation, Yield and Fracture of Polymers, Cambridge University, April 1994; poster 117.
(21) Steenbrink, A. C.; Janik, H.; Gaymans, R. J. *J. Mater. Sci.* **1997**, *32*, 5505.
(22) Vu-Khanh, T. *Theor. Appl. Fract. Mech.* **1998**, *29*, 75.
(23) Takahashi, K. *J. Polym. Sci., Polym. Phys. Ed.* **1974**, *12*, 1697.
(24) Cessna, L. C. *Polym. Eng. Sci.* **1974**, *14*, 696.
(25) Bucknall, C. B. *Br. Plast.* **1967**, *40*, 84.
(26) Donald, A. M.; Kramer, E. J. J. *Polym. Sci. Polym. Phys. Ed.* **1982**, *20*, 899.
(27) Donald, A. M.; Kramer, E. J. *J. Mater. Sci.* **1982**, *17*, 1871.
(28) Donald, A. M. *J. Mater. Sci.* **1985**, *20*, 2630.
(29) Berger, L. L.; Kramer, E. J. *Macromolecules* **1987**, *20*, 1980.
(30) McLeish, T. C. B.; Plummer, C. J. G.; Donald, A. M. *Polymer* **1989**, *30*, 1651.
(31) Plummer, C. J. G.; Donald, A. M. *Macromolecules* **1990**, *23*, 3929.
(32) Donald, A. M.; Kramer, E. J. *J. Appl. Polym. Sci.* **1982**, *27*, 3729.
(33) Piorkowska, E.; Argon, A. S.; Cohen, R. E. *Macromolecules* **1990**, *23*, 3838.
(34) Moore, J. D. *Polymer* **1971**, *12*, 478.
(35) Silberberg, J.; Han, C. D. *J. Appl. Polym. Sci.* **1978**, *22*, 599.
(36) Bucknall, C. B.; Davies, P.; Partridge, I. K. *J. Mater. Sci.* **1987**, *22*, 1341.
(37) Cook, D. G.; Rudin, A.; Plumtree, A. *J. Appl. Polym. Sci.* **1993**, *48*, 75.
(38) Dağli, G.; Argon, A. S.; Cohen, R. E. *Polymer* **1995**, *36*, 2173.
(39) Argon, A. S.; Cohen, R. E.; Gebizlioglu, O. S. In *Toughening of Plastics-II*; Bucknall, C. B., Ed.; Plastics and Rubber Institute: London, 1984; p 21/1.
(40) Brown, H. R.; Argon, A. S.; Cohen, R. E.; Gebizlioglu, O. S.; Kramer, E. J. *Macromolecules* **1989**, *22*, 1002.
(41) Piorkowska, E.; Argon, A. S.; Cohen, R. E. *Polymer* **1993**, *34*, 4435.

MA0109424